Journal of Computational Physics **176,** 295–329 (2002)
doi:10.1006/jcph.2001.6986, available online at http://www.idealibrary.com on IDEAL®

Numerical Study of Quantum Resonances in Chaotic Scattering

Kevin K. Lin[1]

Department of Mathematics, University of California, Berkeley, California 94720
E-mail: kkylin@math.berkeley.edu

Received May 22, 2001; revised December 10, 2001

This paper presents numerical evidence that in quantum systems with chaotic classical dynamics, the number of scattering resonances near an energy E scales like $\hbar^{-(D(K_E)+1)/2}$ as $\hbar \to 0$. Here, K_E denotes the subset of the energy surface $\{H = E\}$ which stays bounded for all time under the flow generated by the classical Hamiltonian H and $D(K_E)$ denotes its fractal dimension. Since the number of bound states in a quantum system with n degrees of freedom scales like $\hbar^{-n}$, this suggests that the quantity $(D(K_E) + 1)/2$ represents the effective number of degrees of freedom in chaotic scattering problems. The calculations were performed using a recursive refinement technique for estimating the dimension of fractal repellors in classical Hamiltonian scattering, in conjunction with tools from modern quantum chemistry and numerical linear algebra.

Key Words: scattering resonances; semiclassical asymptotics; chaotic trapping; fractal dimension.

1. INTRODUCTION

Quantum mechanics identifies the energies of stationary states in an isolated physical system with the eigenvalues of its Hamiltonian operator. Because of this, eigenvalues play a central role in the study of bound states, such as those describing the electronic structures of atoms and molecules [6]. When the corresponding classical system allows escape to infinity, resonances replace eigenvalues as fundamental quantities: The presence of a resonance at $\lambda = E - i\gamma$, with E real and $\gamma > 0$, gives rise to a dissipative metastable state with energy E and decay rate γ [38]. Such states are essential in scattering theory, as well as in models of dissipative phenomena such as radiative damping. This paper is concerned with resonances in the scattering setting.

[1] Supported by the Fannie and John Hertz Foundation.

0021-9991/02 $35.00

An important property of energy eigenvalues is that one can count them using only the classical Hamiltonian function $H(x, p) = \frac{1}{2}\|p\|^2 + V(x)$ and Planck's constant $\hbar$: For fixed energies $E_0 < E_1$, the number $N_{\text{eig}}(E_0, E_1, \hbar)$ of eigenvalues in $[E_0, E_1]$ satisfies

$$N_{\text{eig}}(E_0, E_1, \hbar) \approx \frac{\text{vol}(\{E_0 \le H \le E_1\})}{(2\pi\hbar)^n}, \tag{1}$$

where n denotes the number of degrees of freedom and vol$(\cdot)$ phase space volume. This result, known as the *Weyl law* [8, 17], expresses the density of quantum states using the classical Hamiltonian function. No direct generalization to resonances is currently known.

In this paper, numerical evidence for a Weyl-like power law is presented for resonances in a two-dimensional model with three symmetrically placed gaussian potentials. A conjecture, based on the work of Sjöstrand [28] and Zworski [36], states that the number of resonances $\lambda = E - i\gamma$ with $E_0 < E < E_1$ and $0 < \gamma < \hbar$ asymptotically lies between $C_1\hbar^{-(D(K_{E_1})+1)/2}$ and $C_0\hbar^{-(D(K_{E_0})+1)/2}$ as $\hbar \to 0$, where

$$\begin{aligned} D(\cdot) &= \text{dimension (see below)}, \\ K_E &= K \cap \{H = E\}, \\ K &= \{(x, p) : \sup_t \|\Phi_t(x, p)\| < \infty\}, \\ \Phi_t &= \text{flow generated by } H. \end{aligned} \tag{2}$$

If $D(K_E)$ depends continuously on E and $|E_1 - E_0|$ is sufficiently small, then $D(K_{E_1}) \approx D(K_{E_0})$ and the number of resonances in such a region is comparable to $\hbar^{-(D(K_E)+1)/2}$ for any $E \in [E_0, E_1]$. As the conjecture links quantum and classical dynamics, its numerical verification requires that one calculate both resonances and trapped set dimensions.

The sets K and K_E, called *trapped sets*, consist of initial conditions which generate trajectories that stay bounded forever. In systems where $\{H \le E\}$ is bounded for all E, the conjecture reduces to the Weyl asymptotic $\hbar^{-n}$. Note that the conjecture implies that

$$\text{effective number of degrees of freedom for metastable states} = \frac{D(K_E) + 1}{2} \tag{3}$$

for both quantum and classical chaotic scattering. In this paper, the term "chaotic" always means *hyperbolic*; see Sjöstrand [28] or Gaspard [13] for definitions.

The notion of dimension requires some comment: The "triple gaussian" model considered here has very few trapped trajectories, and K and K_E (for any energy E) have vanishing Lebesgue measures. Thus, $D(K)$ is strictly less than $2n = 4$ and $D(K_E) < 2n - 1 = 3$. In fact, the sets K and K_E are fractal, as are trapped sets in many other chaotic scattering problems. This leads to the question of which dimension to use—a difficult question which requires further study.

This paper is organized as follows: First, the model system is defined. This is followed by mathematical background information and a heuristic argument for the conjecture. Then, numerical methods for computing resonances and fractal dimensions are developed, and numerical results are presented and compared with known theoretical predictions.

2. TRIPLE GAUSSIAN MODEL

The model system has $n = 2$ degrees of freedom; its phase space is R^4, whose points are denoted by (x, y, p_x, p_y).

First, it is convenient to define

$$G^{\sigma}_{x_0}(x) = \exp\left(-\frac{(x-x_0)^2}{2\sigma^2}\right). \tag{4}$$

Similarly, put

$$G^{\sigma}_{(x_0,y_0)}(x,y) = \left(G^{\sigma}_{x_0} \otimes G^{\sigma}_{y_0}\right)(x,y) = G^{\sigma}_{x_0}(x) \cdot G^{\sigma}_{y_0}(y) \tag{5}$$

in two dimensions.

Now, define H by

$$H(x, y, p_x, p_y) = \frac{p_x^2 + p_y^2}{2} + V_3(x, y), \tag{6}$$

where the potential V_m is given by

$$\begin{aligned} V_m &= \sum_{k=1}^{m} G^{\sigma}_{c(k,m)}, \\ c(k,m) &= \left(R\cos\left(\frac{2\pi k}{m}\right), R\sin\left(\frac{2\pi k}{m}\right)\right). \end{aligned} \tag{7}$$

That is, it consists of m gaussian "bumps" placed at the vertices of a regular m-gon centered at the origin, at a distance $R > 0$. This paper focuses on the case $m = 3$ because it is the simplest case that exhibits nontrivial dynamics in two dimensions. However, the case $m = 2$ is also relevant because it is well understood: See Miller [22] for early heuristic results and Gérard and Sjöstrand [14] for a rigorous treatment. Thus, double gaussian scattering serves as a useful test case for the techniques described here.

The quantized Hamiltonian $\hat{H}$ is similarly defined:

$$\hat{H} = -\frac{\hbar^2}{2}\Delta + V_3. \tag{8}$$

See Fig. 1.

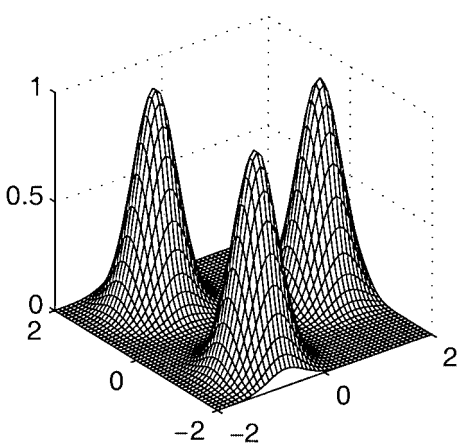

FIG. 1. The triple gaussian potential. Here, $R = 1.4$ and $\sigma = 1/3$.

3. BACKGROUND

The section provides a general discussion of resonances and motivates the conjecture in the context of the triple gaussian model. However, most of the definitions and arguments here carry over to more general systems with n degrees of freedom, and the notation has been chosen accordingly. The reader should keep in mind that $n = 2$ for the triple gaussian model.

There exists an extensive literature on resonances and semiclassical asymptotics in other settings. For example, see [10–12, 35] for detailed studies of the classical and quantum mechanics of hard disc scattering.

3.1. Resonances

Resonances can be defined mathematically as follows: Set $R(z) = (\hat{H} - zI)^{-1}$ for real z, where I is the identity operator. This one-parameter family of operators $R(z)$ is the *resolvent* and is meromorphic with suitable modifications of its domain and range. The poles of its continuation into the complex plane are, by definition, the *resonances* of $\hat{H}$ [38].

Less abstractly, resonances are generalized eigenvalues of $\hat{H}$. Thus, we should solve the *time-independent Schrödinger equation*

$$\hat{H}\psi = \lambda\psi \tag{9}$$

to obtain the resonance λ and its generalized eigenfunction ψ. In bound state computations, one approximates ψ as a finite linear combination of basis functions and solves a finite-dimensional version of the equation above. For similar calculations to be carried out for resonances, it is necessary that ψ lie in a function space which facilitates such approximations, for example L^2.

Let ψ and λ solve (9). Then $e^{-(i/\hbar)\lambda t} \cdot \psi$ solves the *time-dependent Schrödinger equation*

$$i\hbar\frac{\partial\psi}{\partial t} = \hat{H}\psi. \tag{10}$$

Since metastable states decay in time, $\mathrm{Im}(\lambda)$ must be negative. Now suppose, for simplicity, that $n = 1$ (the analysis in higher dimensions requires more care, though the result is the same): A plane wave with energy E coming in from $-\infty$ produces a transmitted wave $\psi(x) \approx Ce^{(i/\hbar)\sqrt{2E}x}$ for large positive x. Substituting $\lambda = E - i\gamma$ for E yields $e^{(i/\hbar)\sqrt{2\lambda}x}$, which grows exponentially as $x \to +\infty$ because $\mathrm{Im}(\sqrt{E - i\gamma}) < 0$. Finite rank approximations of $\hat{H}$ cannot capture such generalized eigenfunctions. However, if we make the formal substitution $x \mapsto xe^{i\alpha}$, then the wave function becomes $\exp(\frac{i}{\hbar}\sqrt{2\lambda} \cdot e^{i\alpha}x)$. Choosing $\alpha > \frac{1}{2}\tan^{-1}(\gamma/E)$ forces ψ to decay exponentially.

This procedure, called *complex scaling*, transforms the Hamiltonian operator $\hat{H}$ into the *scaled operator* $\hat{H}_\alpha$. It also maps metastable states ψ with decay rate $\gamma < E\tan(2\alpha)$ to genuine L^2 eigenfunctions ψ_α of $\hat{H}_\alpha$. The corresponding resonance λ becomes a genuine eigenvalue: $\hat{H}_\alpha\psi_\alpha = \lambda\psi_\alpha$. Furthermore, resonances of $\hat{H}$ will be invariant under small perturbations in α, whereas other eigenvalues of $\hat{H}_\alpha$ will not. The condition $\alpha > \frac{1}{2}\tan^{-1}(\gamma/E)$ implies that, for small γ and fixed E, the method will capture a resonance $\lambda = E - i\gamma$ if and only if $\gamma < 2E\alpha + O(\alpha^2)$. We can perform complex scaling in higher dimensions by substituting $r \mapsto re^{i\alpha}$ in polar coordinates.

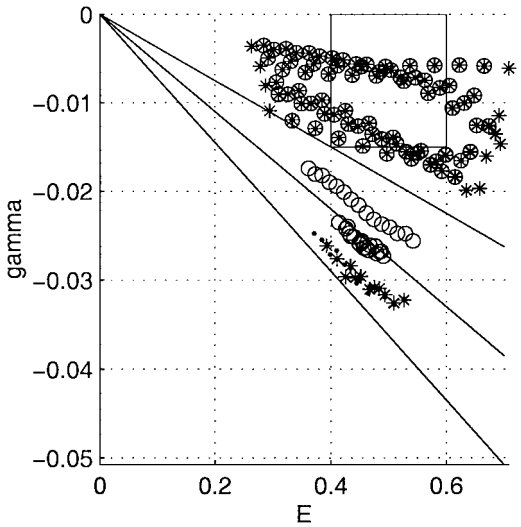

FIG. 2. Illustration of complex scaling: The box at the top of the figure is the region of interest; only resonances in that box are counted. Under complex scaling, the continuous spectrum (corresponding to "unbound states") of $\hat{H}$ is rotated into the lower half plane. The three diagonal lines indicate where the rotated continuous spectra for different values of α *should* be: Although most eigenvalues of $\hat{H}_\alpha$ actually belong to the scaled continuous spectrum, they do not appear here because only eigenvalues near the region of interest are computed. (A few do appear near the diagonal lines.) Filled circles mark resonances, while stars, empty circles, and dots mark other eigenvalues of $\hat{H}_\alpha$.

In algorithmic terms, this means we can compute eigenvalues of $\hat{H}_\alpha$ for a few different values of α and look for invariant values, as demonstrated in Fig. 2. In addition to its accuracy and flexibility, this is one of the advantages of complex scaling: The invariance of resonances under perturbations in α provides an easy way to check the accuracy of calculations, mitigating some of the uncertainties inherent in computational work. Note that the scaled operator $\hat{H}_\alpha$ is no longer self-adjoint, which results in non-hermitian finite-rank approximations and complex eigenvalues.

This method, first introduced for theoretical purposes by Aguilar and Combes [1] and Balslev and Combes [4], was further developed by Simon in [27]. It has since become one of the main tools for computing resonances in physical chemistry [23, 25, 32, 33]. For recent mathematical progress, see [19, 28, 29] and references therein. Interested readers are also referred to [34] and references there for a different approach to resonance computation.

For reference, the scaled triple gaussian operator $\hat{H}_\alpha$ is

$$\hat{H}_\alpha = -e^{-2i\alpha} \cdot \frac{\hbar^2}{2}\Delta + V_{3,\alpha}, \tag{11}$$

where

$$\begin{aligned} V_{m,\alpha} &= \sum_{k=1}^{m} G^{\sigma_\alpha}_{c_\alpha(k,m)}, \\ \sigma_\alpha &= e^{-i\alpha} \cdot \sigma, \\ c_\alpha(k,m) &= e^{-i\alpha} c(k,m). \end{aligned} \tag{12}$$

Note that these expressions only make sense because $G^{\sigma}_{x_0}(x)$ is analytic in x, x_0, and σ.

3.2. Fractal Dimension

As the Minkowski dimension arises naturally in the heuristic argument in the next section, let us recall its definition: The *Minkowski dimension* of a set $U \subset R^m$ is

$$D = \inf\left\{d : \limsup_{\epsilon \to 0}(\epsilon^{d-m} \cdot \mathrm{vol}(U_\epsilon)) < \infty\right\}, \tag{13}$$

where $U_\epsilon = \{y \in R^m : \mathrm{dist}(y, U) < \epsilon\}$. A simple calculation yields

$$D(U) = \lim_{\epsilon \to 0} \frac{\log(\mathrm{vol}(U_\epsilon)/\epsilon^m)}{\log(1/\epsilon)} \tag{14}$$

when the limit exists.

In studying fractal sets and measures, one can employ many different definitions of dimension; the Minkowski dimension is certainly not unique. Furthermore, it has some unfortunate properties. For example, a countable union of zero-dimensional sets can have positive Minkowski dimension. For this reason, texts on the theory of dimensions typically begin with the better-behaved Hausdorff dimension. But the Minkowski dimension is sometimes easier to manipulate and almost always easier to compute.

For a detailed treatment of different definitions of dimension and their applications in the study of dynamical systems, see [9, 24].

3.3. Generalizing the Weyl Law

Equation (1) makes no sense for scattering resonances because the volume on the right-hand side is infinite for most choices of E_0 and E_1. This seems to mean that there is no generalization of the Weyl law in the setting of scattering theory. However, the following heuristic argument suggests otherwise:

As mentioned before, a metastable state corresponding to a resonance $\lambda = E - i\gamma$ has a time-dependent factor of the form $e^{-(i/\hbar)\lambda t} = e^{-(i/\hbar)Et} \cdot e^{-(\gamma/\hbar)t}$. A wave packet whose dynamics is dominated by λ (and other resonances near it) would therefore exhibit temporal oscillations of frequency $O(E/\hbar)$ and lifetime $O(\hbar/\gamma)$. Heuristically, then, the number of times the particle bounces in the trapping region formed by the gaussian bumps should be comparable to $\frac{E}{\hbar} \cdot \frac{\hbar}{\gamma} = \frac{E}{\gamma}$.

In the semiclassical limit, the motion of the wave packet should be well-approximated by the underlying classical dynamics. Let $T(x, y, p_x, p_y)$ denote the time to escape the trapping region from the initial phase point (x, y, p_x, p_y). The diameter of the trapping region is $O(R)$, and typical velocities in the energy surface $\{H = E\}$ are $O(E^{1/2})$ (mass is set to 1), so the number of times a classical particle bounces before escaping should be $O(T\sqrt{E}/R)$. This suggests that, in the limit $\hbar \to 0$, $T\sqrt{E}/R \sim E/\gamma$ and consequently

$$T \sim \frac{R\sqrt{E}}{\gamma}. \tag{15}$$

Fix $\gamma_0 > 0$, and consider

$$N_{\mathrm{res}} = \#\{E - i\gamma : E_0 \le E \le E_1, \gamma \le \gamma_0\} \tag{16}$$

for fixed energies E_0 and E_1: Equations (15) and (16) imply that $T \geq R\sqrt{E_0}/\gamma_0$, so by analogy with the Weyl law,

$$\frac{\mathrm{vol}\left(\left\{E_0 \leq H \leq E_1, T \geq \frac{R\sqrt{E_0}}{\gamma_0}\right\}\right)}{(2\pi\hbar)^n} \tag{17}$$

follows as an approximation for the number of quantum states with the specified energies and decay rates.

Now, the function $1/T$ is nonnegative for all (x, y, p_x, p_y) and vanishes on $K_{[E_0,E_1]} = K \cap \{E_0 \leq H \leq E_1\}$. Assuming that $1/T$ is sufficiently regular,[2] this suggests

$$1/T(x, y, p_x, p_y) \sim d_{K_{[E_0,E_1]}}(x, y, p_x, p_y)^2, \tag{18}$$

where $d_{K_{[E_0,E_1]}}$ denotes distance to $K_{[E_0,E_1]}$. It follows that N_{res} should scale like

$$\frac{\mathrm{vol}\left(\left\{E_0 \leq H \leq E_1, d_{K_{[E_0,E_1]}} \leq \gamma_0^{1/2}\right\}\right)}{\hbar^n}. \tag{19}$$

For small γ_0, this becomes

$$C(R, E_0, E_1) \cdot \hbar^{-n} \cdot \gamma_0^{\frac{2n-D(K_{[E_0,E_1]})}{2}} \tag{20}$$

for some constant C, by (13). Setting $\gamma_0 = \hbar$ and assuming that $D(K_E)$ decreases monotonically with increasing E (as is the case in Fig. 22) yields

$$C_1\hbar^{-\frac{D(K_{E_1})+1}{2}} \leq N_{\mathrm{res}} \leq C_0\hbar^{-\frac{D(K_{E_0})+1}{2}}. \tag{21}$$

If $|E_1 - E_0|$ is sufficiently small, then $D(K_{[E_0,E_1]}) \approx D(K_E) + 1$ for $E \in [E_0, E_1]$, and

$$N_{\mathrm{res}} \sim \hbar^{-\frac{D(K_E)+1}{2}}. \tag{22}$$

In [28], Sjöstrand proved the following rigorous upper bound: For $\gamma_0 > 0$ satisfying $C\hbar < \gamma_0 < 1/C$,

$$N_{\mathrm{res}} = O\left(C_\delta\hbar^{-n}\gamma_0^{\frac{2n-D(K_{[E_0,E_1]})+\delta}{2}}\right) \tag{23}$$

holds for all $\delta > 0$. When the trapped set is of *pure dimension*, that is when the infimum in Eq. (13) is achieved, one can take $\delta = 0$. Setting $\gamma_0 = \hbar$ gives an upper bound of the form (22).

In his proof, Sjöstrand used the semiclassical argument above with escape functions and the Weyl inequality for singular values. Zworski continued this work in [36], where he proved

[2] In fact, this is numerically self-consistent: Assume that $1/T$ vanishes to order ν (with ν not necessarily equal to 2) on K, and *assume* the conjecture. Then the number of resonances would scale like $\hbar^{(2n-D(K))/\nu}$, from which one can solve for ν. With the numerical data obtained here, this indeed turns out to be 2 (but with some fluctuations). If $1/T$ does not vanish quadratically *everywhere* on K, variations in its regularity may affect the correspondence between classical trapping and the distribution of resonances.

a similar result for scattering on convex co-compact hyperbolic surfaces with no cusps. His work was motivated by the availability of a large class of examples with hyperbolic flows, easily computable dimensions, and the hope that the Selberg trace formula could help obtain lower bounds. But these hopes remain unfulfilled so far [15], and that partly motivates this work.

4. COMPUTING RESONANCES

Complex scaling reduces the problem of calculating resonances to one of computing eigenvalues. What remains is to choose scaling angles α, approximate $\hat{H}_\alpha$ by rank N matrices $\hat{H}_{N,\alpha}$ for each α, and compute their spectra numerically. For comparison, see [23, 25, 32, 33] for applications of complex scaling to problems in physical chemistry.

4.1. Choice of Scaling Angle

To count resonances in the box $[E_0, E_1] - i[0, \hbar]$, it is necessary to choose $\alpha \geq \tan^{-1}(\frac{\hbar}{E_0})$ so that the corresponding generalized eigenfunction can be captured by finite rank approximations (see Fig. 2 and Section 3.1). The resonance calculation described here uses the smallest acceptable value,

$$\alpha = \tan^{-1}\left(\frac{\hbar}{E_0}\right), \tag{24}$$

so that $\alpha = O(\hbar)$ as $\hbar \to 0$. In addition to satisfying $\alpha \geq \tan^{-1}(\frac{\hbar}{E_0})$, this choice keeps the scaled operator $\hat{H}_\alpha$ nearly normal. Near-normality, in turn, helps avoid possible pseudospectral effects, which can interfere with eigenvalue calculations [31, 37]:

Let A be an operator on a Hilbert space, and let $R(z)$ be the resolvent $(A - zI)^{-1}$. When A is *normal*, that is, when A commutes with its adjoint A^*, the spectral theorem applies and the inequality

$$\|R(z)\| = \|(A - zI)^{-1}\| \leq \operatorname{dist}(z, \sigma(A))^{-1} \tag{25}$$

holds ($\sigma(A)$ denotes the spectrum of A). When A is nonnormal, as is the case for $\hat{H}_\alpha$, no such inequality holds and $\|R(z)\|$ can become very large for z far from $\sigma(A)$. Trefethen demonstrates in [31] that numerical algorithms often compute *false eigenvalues* in such regions, where the resolvent becomes large far from the true spectrum.

More precisely, let us define the *ϵ-pseudospectrum* as

$$\Lambda_\epsilon(A) = \{z : \|R(z)\| \geq 1/\epsilon\}. \tag{26}$$

When A is a matrix, it is easy to show that

$$\Lambda_\epsilon(A) = \{z : \exists A' \text{ such that } z \in \sigma(A + A'),\ \|A'\| \leq \epsilon\}. \tag{27}$$

That is, the ϵ-pseudospectrum of A consists of those complex numbers z which are eigenvalues of an ϵ-perturbation of A. The notion of pseudospectra can be extended to general linear operators.

In [37], Zworski explains pseudospectral phenomenon using semiclassical asymptotics. Roughly speaking, there exist $\epsilon = \epsilon(\hbar)$ such that the closure of the range of the *scaled Hamiltonian function* H_α,

$$H_\alpha(x, y, p_x, p_y) = e^{-2i\alpha} \cdot \frac{p_x^2 + p_y^2}{2} + V_{3,\alpha}, \tag{28}$$

is contained in the $\epsilon(\hbar)$-pseudospectrum of the scaled operator $\hat{H}_\alpha$, with $\epsilon(\hbar) = O(\hbar^N)$ as $\hbar \to 0$ for all $N > 0$. In the present setting, a simple calculation shows that for small α, range (H_α) contains the box $[E_0, E_1] - i[0, \hbar]$ for $E_0 = 0.4$, $E_1 = 0.6$. Thus, it is desirable to choose the smallest acceptable α to make $\hat{H}_\alpha$ as near-normal as possible. Also, as illustrated by Figs. 31–34, the invariance of resonances under perturbations in α helps filter out some pseudospectral effects.

4.2. Eigenvalue Computation

Suppose that we have constructed $\hat{H}_{N,\alpha}$. Instead of solving the eigenvalue problem $\hat{H}_{N,\alpha} v = \lambda v$ directly, it is natural to solve the equivalent eigenvalue problem

$$(\hat{H}_{N,\alpha} - \lambda_0)^{-1} v = \lambda' v. \tag{29}$$

Efficient implementations of the Arnoldi or Lanczos algorithms (see [20] and references therein) can solve for the largest few eigenvalues λ' of $(\hat{H}_{N,\alpha} - \lambda_0)^{-1}$ using relatively little auxiliary storage. But $\lambda = \lambda_0 + 1/\lambda'$, so this method allows one to compute a subset of the spectrum of $\hat{H}_{N,\alpha}$ near a given λ_0.

Such algorithms require a method for applying the matrix $(\hat{H}_{N,\alpha} - \lambda_0)^{-1}$ to a given vector v at each iteration step. In the resonance computation, this is done by solving $(\hat{H}_{N,\alpha} - \lambda_0) w = v$ for w, using the conjugate gradient method on the normal equations (see [5]).[3] The resonance program, therefore, consists of two nested iterative methods: An outer Arnoldi loop and an inner iterative linear solver for $(\hat{H}_{N,\alpha} - \lambda_0) w = v$. This computation uses ARPACK [20], which provides a flexible and efficient implementation of the Arnoldi method.

To compute resonances near a given energy E, the program uses $\lambda_0 = E + ia$, $a > 0$, instead of $\lambda_0 = E$. This helps control the condition number of $\hat{H}_{N,\alpha} - \lambda_0$ and gives better error estimates and convergence criteria.[4]

4.3. Matrix Representations

4.3.1. *Choice of Basis*

While one can discretize the differential operator $\hat{H}_\alpha$ via finite differences, in practice it is better to represent the operator using a basis for a subspace of the Hilbert space L^2. This

[3] That is, instead of solving $Aw = v$, one solves $A^* A w = A^* v$. This is necessary because $\hat{H}_{N,\alpha}$ is non-hermitian, and the conjugate gradient method only works for positive definite matrices. This is not the best numerical method for non-hermitian problems, but it is easy to implement and suffices in this case.

[4] Most of the error in solving the matrix equation $(\hat{H}_{N,\alpha} - \lambda_0) w = v$ concentrates on eigenspaces of $(\hat{H}_{N,\alpha} - \lambda_0)^{-1}$ with large eigenvalues. These are precisely the desired eigenvalues, so in principle one can tolerate inaccurate solutions. However, the calculation requires convergence criteria and error estimates for the linear solver, and using $a > 0$, say $a = 1$, turns out to ensure a relative error of about 10^{-6} after about 17–20 iterations of the conjugate gradient solver. A more accurate (and expensive) computation of resonances is not necessary for the purpose of resonance-counting.

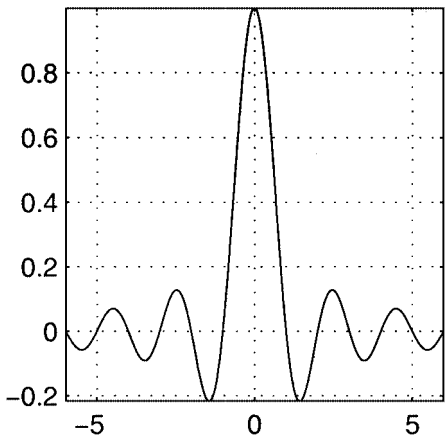

FIG. 3. A sinc function.

should better represent the properties of wave functions near infinity and obtain smaller (but denser) matrices.

Common choices of bases in chemical calculations include so-called "phase space gaussian" [7] and "distributed gaussian" bases [16]. These bases are flexible and are well adapted to calculations involving gaussian or polynomial potentials. However, they are not orthogonal with respect to the standard L^2 inner product, so one must explicitly orthonormalize the basis before computing the eigenvalues of $\hat{H}_{N,\alpha}$. In addition to the computational cost, this requires storing the entire matrix and severely limits the size of the problem one can solve. Instead, this computation uses another well-known class of bases, a *discrete-variable representation* (DVR) [21].

Consider, for the moment, the one-dimensional problem of finding a basis for a "good" subspace of $L^2(R)$. Fix a constant $\Delta x > 0$, and for each integer m, define

$$\phi_{m,\Delta x}(x) = \Delta x^{1/2} \cdot \frac{\sin\left(\frac{\pi}{\Delta x}(x - m\Delta x)\right)}{\pi(x - m\Delta x)}. \tag{30}$$

(This is known as a "sinc" function in engineering literature [26]. See Fig. 3.) The Fourier transform of $\phi_{m,\Delta x}$ is

$$\hat{\phi}_{m,\Delta x}(\omega) = \begin{cases} e^{-im\Delta x} \cdot \Delta x^{1/2}, & |\omega| \le \pi/\Delta x \\ 0, & |\omega| > \pi/\Delta x. \end{cases} \tag{31}$$

One can easily verify that for fixed $\Delta x > 0$, the set $\{\phi_{m,\Delta x}\}$ forms an orthonormal basis for the closed subspace of L^2 functions whose Fourier transforms are supported in $[-\pi/\Delta x, \pi/\Delta x]$.

To find a basis for the corresponding space of band-limited functions in $L^2(R^2)$, simply form the tensor products

$$\phi_{mn}(x_0, y_0) = \phi_{m,\Delta x}(x)\phi_{n,\Delta y}(y). \tag{32}$$

The basis has a natural one-to-one correspondence with points $(m\Delta_1 + X_0, n\Delta_2 + Y_0)$ on a regular lattice of grid points in a box $[X_0, X_1] \times [Y_0, Y_1]$ covering the spatial region of interest. (See Fig. 4.)

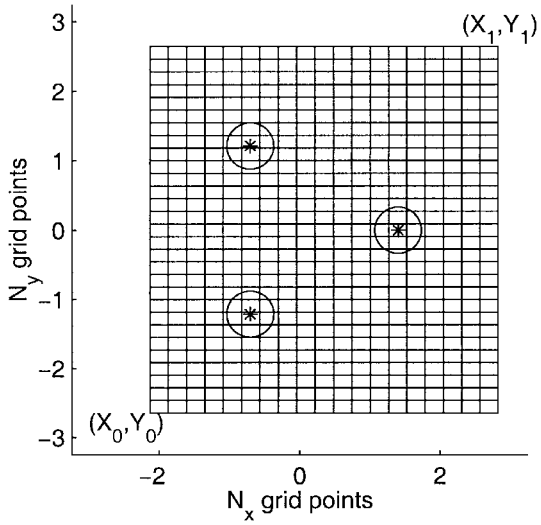

FIG. 4. Illustration of resonance program parameters in configuration space: The lower left corner of the grid is (X_0, Y_0), while the upper right corner is (X_1, Y_1). The grid contains $N_x \times N_y$ points, and a basis function ϕ_{mn} is placed at each grid point. Stars mark potential centers, the circles have radius $\sigma = 1/3$, and $R = 1.4$. Parameters for the classical computation are depicted in Fig. 5.

4.3.2. *Tensor Product Structure*

In the case of energy eigenvalues, the Weyl law states that $N_{\text{eig}} = O(\hbar^{-2})$ as $\hbar \to 0$, since our system has $n = 2$ degrees of freedom. Thus, in order to capture a sufficient number of eigenvalues, the rank N of the matrix approximation must scale like $\hbar^{-2}$. In the absence of more detailed information on the density of resonances, the resonance computation requires a similar assumption to ensure sufficient numerical resolution. This means that for moderately small $\hbar$, the matrix has $N^2 \sim \hbar^{-4}$ entries, which can rapidly become prohibitive on most computers available today.

To reduce storage requirements and running time, one can exploit the separability of the Hamiltonian: Each term in the scaled Hamiltonian $\hat{H}_\alpha$ splits into a tensor product,

$$\frac{\partial^2}{\partial x^2} = \frac{d^2}{dx^2} \otimes I_y, \tag{33}$$

$$\frac{\partial^2}{\partial y^2} = I_x \otimes \frac{d^2}{dy^2}, \tag{34}$$

$$G^\sigma_{(x_0, y_0)} = G^\sigma_{x_0} \otimes G^\sigma_{y_0}, \tag{35}$$

where I_x and I_y denote identity operators on copies of $L^2(R)$. Since the basis $\{\phi_{mn}\}$ consists of tensor products of one-dimensional bases, $\hat{H}_{N,\alpha}$ is also a short sum of tensor products. Thus, if we let N_x denote the number of grid points in the x direction and let N_y denote the number of grid points in the y direction, then $N = N_x \cdot N_y$ and $\hat{H}_{N,\alpha}$ is a sum of five matrices of the form $A_x \otimes A_y$, where A_x has size $N_x \times N_x$ and A_y has size $N_y \times N_y$.

Such tensor products of matrices can be applied to arbitrary vectors efficiently using the outer product representation:[5] On an $N_x \times N_y$ grid, the rank of $\hat{H}_{N,\alpha}$ is $N = N_x \cdot N_y$.

[5] The tensor product of two column vectors v and w can be represented as vw^T. We then have $(A \otimes B) \times (v \otimes w) = (Av) \cdot (Bw)^T$, which extends by linearity to $(A \otimes B)u = AuB^T$.

As $N_x \approx N_y \approx \sqrt{N}$ in these calculations, we can store the tensor factors of the matrix $\hat{H}_{N,\alpha}$ using $O(N_x^2 + N_y^2) = O(N)$ storage instead of $O(N^2)$. Furthermore, while matrix–vector multiplications usually require $O(N^2)$ operations, this tensor product representation requires $O(N_x^3 + N_y^3) = O(N^{3/2})$, a moderate improvement.

Note that this basis fails to take advantage of the discrete rotational symmetry of the triple gaussian Hamiltonian, and the resulting matrix is not sparse, as one can see from the matrix elements for the Laplacian below. Nevertheless, the tensor decomposition provides sufficient compression of information to facilitate efficient computation.

4.3.3. *Matrix Elements*

It is straightforward to calculate matrix elements $K_{mn} = \langle -\frac{\hbar^2}{2}\phi''_{n,\Delta x}, \phi_{m,\Delta x}\rangle$ for the Laplacian on R^1:

$$K_{mn} = \begin{cases} \frac{\hbar^2\pi^2}{\Delta x^2}, & m = n \\ (-1)^{m-n} \cdot \frac{\hbar^2}{\Delta x^2 \cdot (m-n)^2}, & m \neq n. \end{cases} \tag{36}$$

There is no closed form expression for the matrix elements of the potential, but it is easy to perform numerical quadrature with these functions. For example, to compute

$$V_{mn} = \int G(x)\phi_m(x)\phi_n(x)\,dx \tag{37}$$

for $G(x) = e^{-x^2/2\sigma^2}$, one computes

$$V_{mn} \approx \sum_{k=-N}^{N} G(k\delta) \cdot \delta \cdot \phi_m(k\delta) \cdot \phi_n(k\delta), \tag{38}$$

where the stepsize δ should satisfy $\delta \leq \Delta x/2$. It is easy to show that the error is bounded by the sum of

$$2\exp\left(-\frac{|\sigma|^2\pi^2}{2\delta^2}\right), \tag{39}$$

which controls the *aliasing error*, and

$$\frac{(2\pi)^{\frac{1}{2}}|\sigma|}{\Delta x}\exp\left(-\frac{(N-1)^2\delta^2}{2|\sigma|^2}\right), \tag{40}$$

which controls the *truncation error.*

4.3.4. *Other Program Parameters*

The grid spacings Δx and Δy imply a limit on the maximum possible momentum in a wave packet formed by this basis. In order to obtain a finite-rank operator, it is also necessary to limit the number of basis functions.

The resonance computation used the following parameters:

1. X_0, X_1, Y_0, and Y_1 are chosen to cover the region of the configuration space for which $V_3(x, y) \geq 10^{-4}$.

2. Let $L_x = X_1 - X_0$ and $L_y = Y_1 - Y_0$ denote the dimension of the computational domain. The resonance calculation uses $N = N_x \cdot N_y$ basis functions, with $N_x = 1.6 \cdot \frac{L_x\sqrt{8E}}{2\pi\hbar}$ and $N_y = 1.6 \cdot \frac{L_y\sqrt{8E}}{2\pi\hbar}$.

3. This gives

$$\begin{aligned} \Delta x &= L_x/N_x, \\ \Delta y &= L_y/N_y, \end{aligned} \tag{41}$$

which limits the maximum momentum in a wave packet to $|p_x| \le \pi\hbar/\Delta x = 1.6\sqrt{2E}$ and $|p_y| \le \pi\hbar/\Delta y = 1.6\sqrt{2E}$.

5. TRAPPED SET STRUCTURE

5.1. Poincaré Section

Most strategies for computing dimensions involve sampling the ambient space, often on a regular grid, for points which lie "close" to the fractal object of interest. Because the phase space for the triple gaussian model is four-dimensional, a direct calculation of the trapped set can be expensive. The following consideration helps reduce the dimension of the problem:

Recall that R is the distance from each bump to the origin. Around the kth bump, draw a circle C_k of radius $R_0 < R$ (see Fig. 5). Intuitively, if the radius R_0 is sufficiently large, then *most* trapped trajectories will intersect the circles infinitely often. The intersections of these trajectories with the circles should therefore characterize the trapped set, modulo a small subset. The dimension of this intersection should be 1 less than the dimension of the trapped set, because the flow simply pushes this image out along one-dimensional curves.

This leads to the following mathematical construction: Fix an energy E, and choose R_0 so that the C_k do not intersect. Let P_k denote those points (x, y, p_x, p_y) in $\{H = E\}$ such

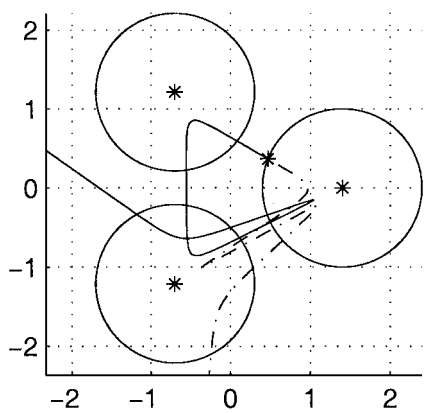

FIG. 5. A typical trajectory. Stars mark the potential centers, whose distance to the origin is $R = 1.4$. The circles have radius $R_0 = 1.0$, and the disjoint union of their cotangent bundles form the Poincaré section. Trajectories start on the circle centered at bump 0 (the bumps are, counterclockwise, 0, 1, and 2) with some given angle θ and angular momentum p_θ. This trajectory generates the finite symbolic sequence $(\infty, 2, 0, 2, \dot{0}, 1, 2, 0, 2, \infty)$. (Symbolic sequences are discussed later in the paper.) The solid curve corresponds to $\Phi_t(\theta, p_\theta)$ for $t \ge 0$, while the dashed curve corresponds to $\Phi_t(\theta, p_\theta)$ for $t < 0$.

that $(x, y) \in C_k$, and let P be the union $P_0 \cup P_1 \cup P_2$. With respect to the kth potential, we can define the *angular momentum* p_θ by

$$p_\theta = \bar{x} \cdot p_y - \bar{y} \cdot p_x, \tag{42}$$

where $\bar{x} = x - R\cos(\theta_k)$, $\bar{y} = y - R\sin(\theta_k)$, and $\theta_k = \frac{2\pi k}{3}$. Similarly, the *radial momentum* is

$$p_r = \left(E - V_3(x, y) - \frac{p_\theta^2}{2R_0^2} \right)^{1/2}. \tag{43}$$

The subspace P_k can be coordinatized by the pair (θ, p_θ) with respect to the kth potential. These coordinates are related to ambient phase space coordinates (x, y, p_x, p_y) by

$$\begin{aligned} x &= R\cos(\theta_k) + R_0\cos(\theta + \theta_k), \\ y &= R\sin(\theta_k) + R_0\sin(\theta + \theta_k), \\ p_x &= p_r\cos(\theta + \theta_k) - \frac{p_\theta}{R_0}\sin(\theta + \theta_k), \\ p_y &= p_r\sin(\theta + \theta_k) - \frac{p_\theta}{R_0}\cos(\theta + \theta_k). \end{aligned} \tag{44}$$

Note that this implicitly embeds P into the energy surface $\{H = E\}$ and that p_r is always chosen to be positive, so that the vector (p_x, p_y) points away from the center of C_k.

Now, take any point (θ, p_θ) in P_k, and form the corresponding point (x, y, p_x, p_y) in R^4 via Eq. (44). Follow along the trajectory $\Phi_t(x, y, p_x, p_y)$. If the trajectory does not escape, it is likely to intersect $C_{k'}$ for some $k' \neq k$, and will generically do so at two points. Let (θ', p'_θ) denote the coordinates (in $P_{k'}$) of the *outgoing intersection*, and set

$$\tilde{\Phi}(\theta, p_\theta, k) = (\theta', p'_\theta, k'). \tag{45}$$

If a trajectory escapes from the trapping region, we can symbolically assign ∞ to $\tilde{\Phi}$.

The map $\tilde{\Phi}$ generates stroboscopic recordings of the flow Φ_t on the submanifold P, and the corresponding discrete dynamical system has trapped set $\tilde{K}_E = K_E \cap P$. As stated before, pushing $\tilde{K}_E$ along the flow Φ_t adds one dimension, so $D(\tilde{K}_E) = D(K_E \cap P) + 1$. By symmetry, we need only compute the dimension of $\tilde{K}_E = K_E \cap P_0$. Since P_0 is two-dimensional, $D(\tilde{K}_E)$ is easier to compute than $D(K_E)$.

Note that the trapped set is naturally partitioned into two subsets: The first consists of trajectories which visit all three bumps, the second of trajectories which bounce between two bumps. The second set forms a one-dimensional subspace of K_E, so the *finite stability* of the Minkowski dimension[6] implies that the second set does not contribute to the dimension of the trapped set.

Readers interested in a more detailed discussion of Poincaré sections and their use in dynamics are referred to [30]. For an application to the similar but simpler setting of hard disc scattering, see [10, 13]. Also, Knauf has applied some of these ideas in a theoretical investigation of classical scattering by Coulombic potentials [18]. Some background material on differentiable manifolds and Hamiltonian mechanics can be found in Arnold [3].

[6] That is, $D(A \cup B) = \max(D(A), D(B))$. For details, see [9].

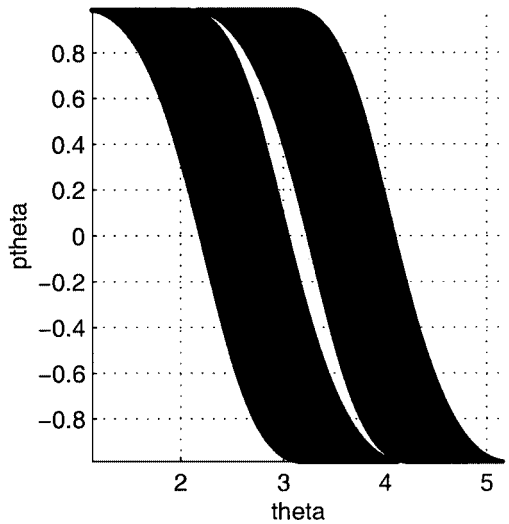

FIG. 6. Points in P_0 which do not go to ∞ after one iteration of $\tilde{\Phi}$. The horizontal axis is θ and the vertical axis is p_θ.

5.2. Self-Similarity

Much is known about the self-similar structure of the trapped set for hard disc scattering [10, 13]; less is known about "soft scatterers" such as the triple gaussian system. However, computational results and analogy with hard disc scattering give strong support to the idea that K (and hence $\tilde{K}_E$) is self-similar or, more precisely, *self-affine*; see Figs. 6–12. (In these images, $E = 0.5$ and $R_0 = 1.0$.) However, it is also clear that, unlike objects such as the Cantor set or the Sierpiński gasket, $\tilde{K}_E$ is not *exactly* self-similar.

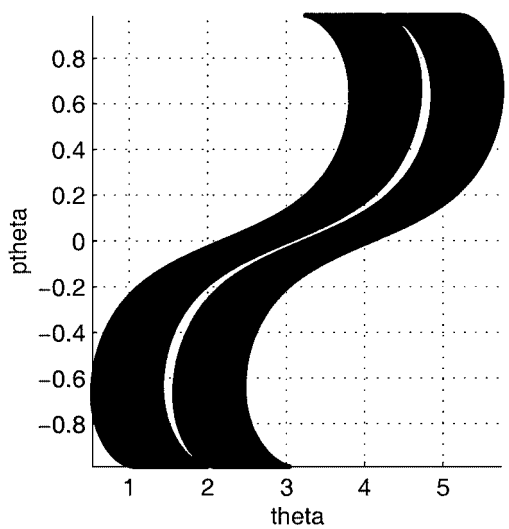

FIG. 7. Points in P_0 which do not go to ∞ after one iteration of $\tilde{\Phi}^{-1}$. The horizontal axis is θ and the vertical axis is p_θ.

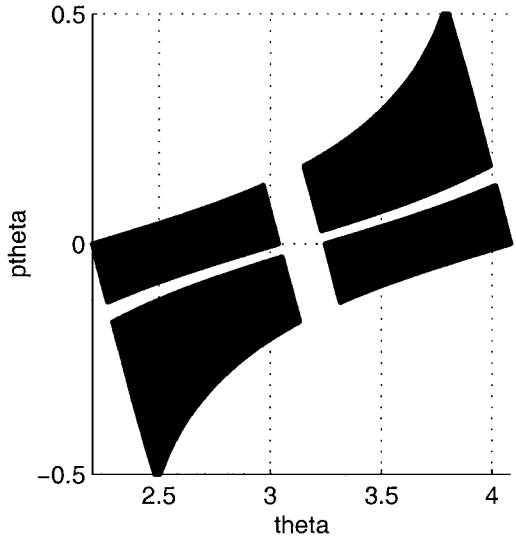

FIG. 8. The intersection of the sets in Figs. 6 and 7. These points correspond to symmetric sequences of length 3 and form the set $\tilde{K}_E^{(1)}$.

5.3. Symbolic Dynamics

The computation of $D(\tilde{K}_E)$ uses symbolic sequences, which requires a brief explanation. Let (θ, p_θ) denote a point in P_0, and consider the trajectory it generates under the flow map Φ_t, for $-\infty < t < \infty$. As explained above, for most choices of (θ, p_θ), the trajectory will cross the circles C_k many times before escaping. (Trapped trajectories will do so infinitely many times.) The sequence of circles that a given trajectory visits form a *symbolic*

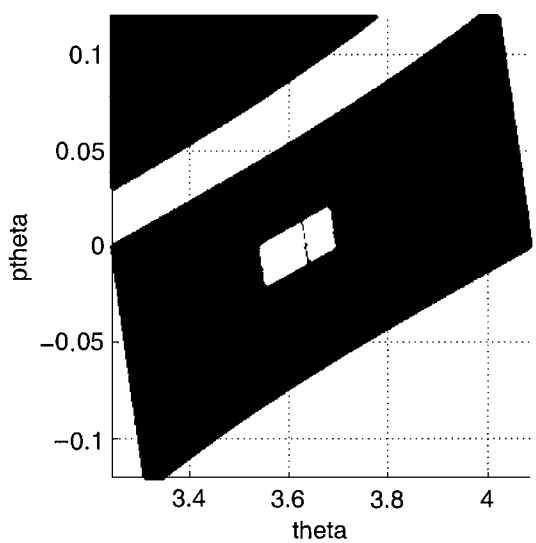

FIG. 9. The lower-right "island" in Fig. 8, magnified. The white cut-out in the middle is the subset corresponding to symmetric sequences of length 5.

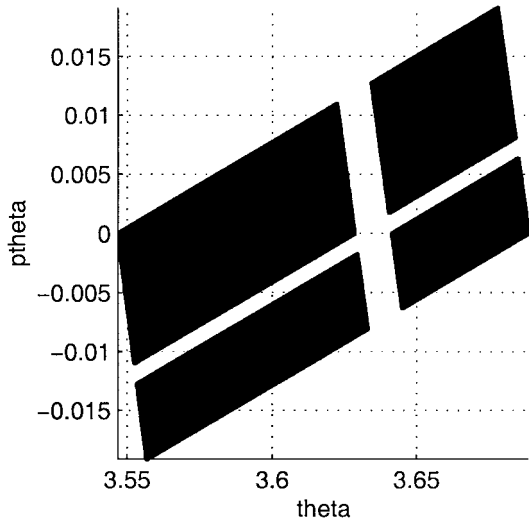

FIG. 10. The cut-out part of Fig. 9, magnified. Recall that these correspond to symmetric sequences of length 5; compare with Fig. 8.

sequence

$$s = (\ldots, s_{-2}, s_{-1}, \dot{0}, s_1, s_2, \ldots), \tag{46}$$

where $\dot{0}$ indicates that the initial point lies in P_0. The integer s_i refers to the circle that the trajectory intersects at the ith iteration of $\tilde{\Phi}$; such sequences satisfy $s_i \in \{0, 1, 2, \infty\}$ and $s_i \neq s_{i+1}$ for all i, with ∞ occurring only at the ends. Sequences satisfying these conditions are *valid*.

For example, the trajectory in Fig. 4 generates the valid sequence

$$(\infty, 2, 0, 2, \dot{0}, 1, 2, 0, 2, \infty). \tag{47}$$

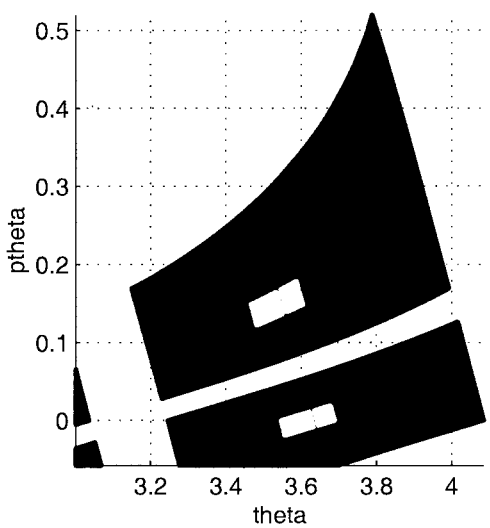

FIG. 11. The upper-right island in Fig. 8. The white cut-out in the middle is, again, the subset corresponding to symmetric sequences of length 5.

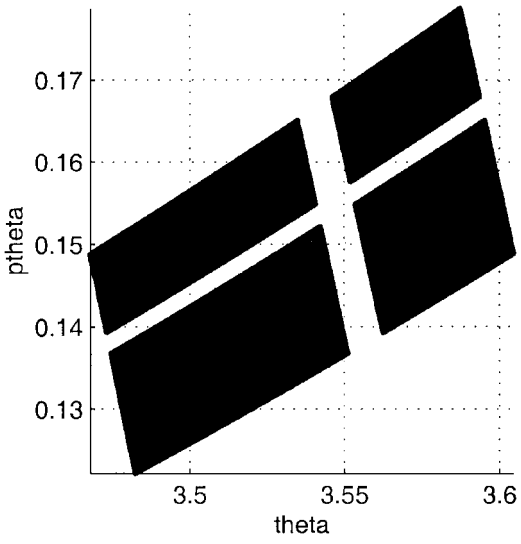

FIG. 12. The cut-out part of Fig. 11, magnified. Recall that these correspond to symmetric sequences of length 5. Compare with Figs. 8 and 10.

Clearly, trapped trajectories generate bi-infinite sequences, whereas escaping trajectories generate finite sequences terminating in the symbol ∞.[7]

Each island in Figs. 8–11 corresponds uniquely to the set of valid sequences containing a specific *symmetric sequence* $(s_{-k}, \ldots, s_{-1}, \dot{0}, s_1, s_2, \ldots, s_k)$. For instance, the four islands in Fig. 8 correspond to the symmetric sequences $(1, \dot{0}, 1)$, $(1, \dot{0}, 2)$, $(2, \dot{0}, 2)$, and $(2, \dot{0}, 1)$. This property is very useful from the computational point of view (see below).

5.4. Dimension Estimates

To compute the Minkowski dimension using Eq. (14), we need to determine when a given point is within ϵ of $\tilde{K}_E$. This is generally impossible. Instead, it is easier to estimate the *information dimension:*

Let $\tilde{K}_E^{(k)}$ denote the set of all points in P_0 corresponding to symmetric sequences of length $2k+1$ centered at 0. That is, $\tilde{K}_E^{(k)}$ consists of all points in P_0 which generate trajectories that bounce at least k times (both forward and backward in time) before escaping. The sets $\tilde{K}_E^{(k)}$ decrease monotonically to $\tilde{K}_E$: $\tilde{K}_E^{(k)} \supset \tilde{K}_E^{(k+1)}$ and $\cap_{k=1}^{\infty} \tilde{K}_E^{(k)} = \tilde{K}_E$.

Now let A_N be and $N \times N$ square grid covering $\tilde{K}_E^{(1)}$ (see Fig. 13); denote its ijth cell by $A_N(i, j)$. Define

$$p_{ij}(N, k) = \frac{\mathrm{vol}\big(\tilde{K}_E^{(k)} \cap A_N(i, j)\big)}{\mathrm{vol}\big(\tilde{K}_E^{(k)}\big)}, \tag{48}$$

where vol$(\cdot)$ denotes phase area in the subspace P_0. Then, the *information dimension* can

[7] In hard disc scattering, the converse holds if R_0/R is sufficiently small: To each bi-infinite valid sequence, there exists a trapped trajectory generating that sequence. This may not hold in the triple gaussian model, and in any case it is not necessary for the computation.

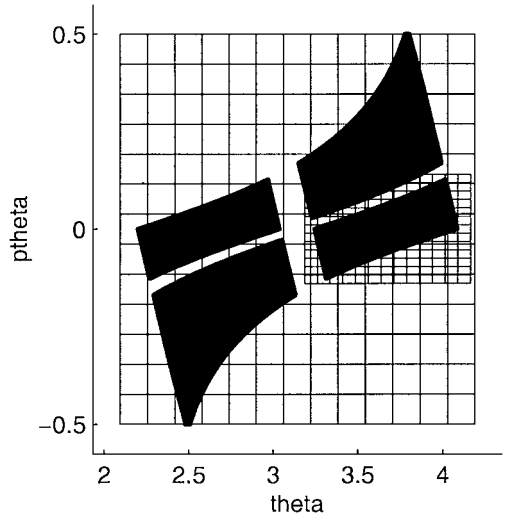

FIG. 13. This figure illustrates the recursive step in the dimension estimation algorithm, showing both the background grid A and an auxiliary grid A'. The grid A remains fixed throughout the computation, but A' is constructed for each island of $\tilde{K}_E^{(k)}$.

be defined by the double limit

$$\lim_{N\to\infty}\lim_{k\to\infty}\frac{-\sum_{ij} p_{ij}(N,k)\log(p_{ij}(N,k))}{\log(N)} \tag{49}$$

in this context. This is actually the information dimension of a probability measure invariant under the Poincaré map $\tilde{\Phi}$. The information dimension of a measure is equal to the Hausdorff dimension of that measure under the condition of *exact dimensionality*, which in turn bounds the Hausdorff dimension of the trapped set from above; these may both differ from the Minkowski dimension of the trapped set [24]. In this paper, the information dimension is taken as an (uncontrolled) estimate of the dimension of the trapped set.

The double limit in Eq. (49) presents a computational problem: In order to calculate the information dimension of the measure, the sets $\tilde{K}_E^{(k)}$ must be approximated on a grid much finer than the $N \times N$ grid A_N. This can be quite time-consuming. The dimension calculation therefore uses a simple adaptive algorithm, where a finer grid is generated recursively on each island of $\tilde{K}_E^{(k_{\text{stop}})}$, where k_{stop} is chosen sufficiently large to approximate the inner limit.

Here is the algorithm:

1. **Set Parameters:** First, fix the following:
   (i) N: number of grid points per axis on the background grid A
   (ii) N': number of grid points per axis on the auxiliary grid
   (iii) k_{stop}: recursion depth
2. **Initialize Background Grid:** Construct the grid A to cover $\tilde{K}_E^{(1)}$; A will remain fixed throughout the computation. Let C be an $N \times N$ integer matrix, all of whose entries are initialized to 0.
3. **Prepare for Recursion:** Set $k = 1$, $A' = A$, and $\sigma = (\dot{0})$ (σ is a symbolic sequence of length 1).
4. **Recursively Refine Grids:**

(i) **Identify Islands:** For each valid sequence of the form $\sigma' = (a, \sigma, b)$ of length $2k + 3$ ($a, b \in \{0, 1, 2\}$), compute the corresponding island $I_{\sigma'}$ on A' by iterating the Poincaré

map $\tilde{\Phi}$ for each grid point of A'. Keep in mind that the set $\tilde{K}_E^{(k)}$ consists of 4^k islands, each corresponding to a unique symmetric sequence σ of length $2k+1$ (see Fig. 8).

(ii) **Magnify and Recurse:** If $k < k_{\text{stop}}$, then repeat Step 4 for each island $I_{\sigma'}$, with A' set to a new $N' \times N'$ grid centered on $I_{\sigma'}$ (see Fig. 13), k set to $k+2$, and σ set to σ'. Otherwise, proceed to the next step.

(iii) **Count:** For each point in each island I_σ (where the length of σ is now $2k_{\text{stop}}+1$), increment the corresponding entry of the matrix C by 1.

5. **Estimate Dimension:** The matrix C lets us estimate

$$\begin{aligned} p_{ij} &= \frac{\text{vol}\left(\tilde{K}_E^{(k_{\text{stop}})} \cap A_{ij}\right)}{\text{vol}\left(\tilde{K}_E^{(k_{\text{stop}})}\right)} \\ &\approx \frac{C_{ij}}{N_{\text{total}}}, \end{aligned} \tag{50}$$

where $N_{\text{total}} = \sum_{ij} C_{ij}$. The quantity

$$\frac{-\sum_{ij} p_{ij} \log(p_{ij})}{\log(N)} \tag{51}$$

is then an estimate of the information dimension.

Figure 13 illustrates the grids used in this algorithm.

6. NUMERICAL RESULTS

6.1. Resonance Counting

As an illustration of complex scaling, Figs. 14–18 contain resonances for $R = 1.4$ and $\hbar \in [0.017, 0.025]$. Eigenvalues of $\hat{H}_{N,\alpha}$ for different values of α are marked by different styles of points, and the box has depth $\hbar$ and width 0.2, with $E_0 = 0.4$ and $E_1 = 0.6$. These plots may seem somewhat empty because only those eigenvalues of $\hat{H}_{N,\alpha}$ in regions of

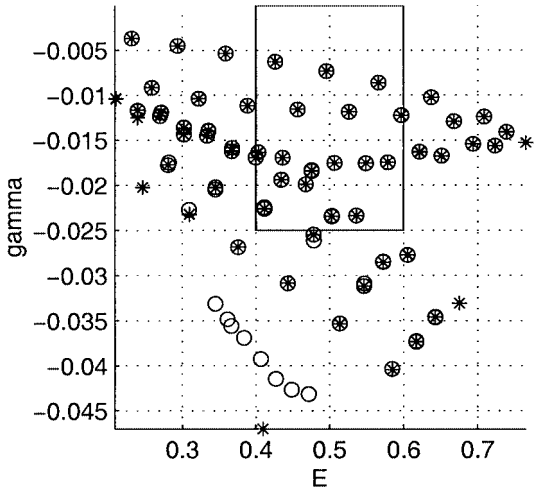

FIG. 14. As in Fig. 2, filled circles mark resonances, while stars, empty circles, and dots mark other eigenvalues of $\hat{H}_\alpha$ for $\alpha \in \{0.0624, 0.0799, 0.0973\}$. The parameters are $E = 0.5$, $\hbar = 0.025$, and $R = 1.4$. This calculation used an 102×108 grid, and 90 out of $N = 11{,}016$ eigenvalues were computed.

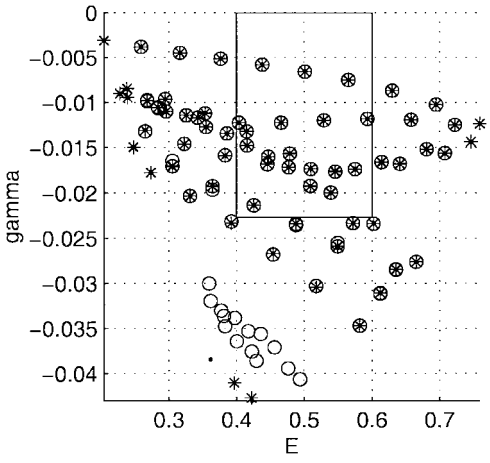

FIG. 15. This plot is the same as Fig. 14, except that $\hbar = 0.022702$ and $\alpha \in \{0.0567, 0.0741, 0.0916\}$. This calculation uses a 112×119 grid and computed 98 out of $N = 13{,}328$ eigenvalues.

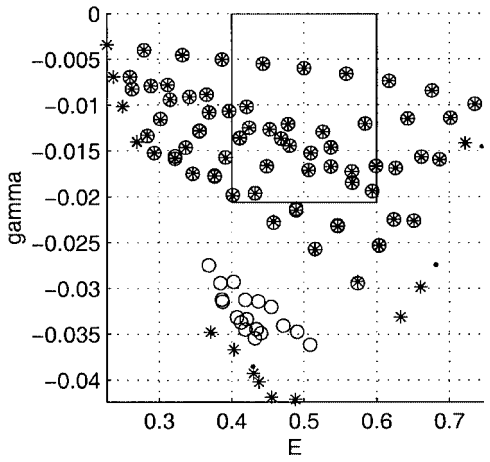

FIG. 16. This calculation uses $\hbar = 0.020616$ and $\alpha \in \{0.0515, 0.0689, 0.0864\}$. It was done on a 123×131 grid, and 107 out of $N = 16{,}113$ eigenvalues were computed.

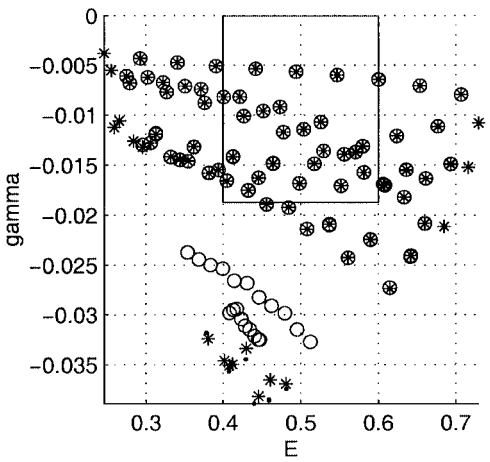

FIG. 17. This calculation uses $\hbar = 0.018721$ and $\alpha \in \{0.0468, 0.0642, 0.0817\}$. It was done on a 135×144 grid, and 116 out of $N = 19{,}440$ eigenvalues were computed.

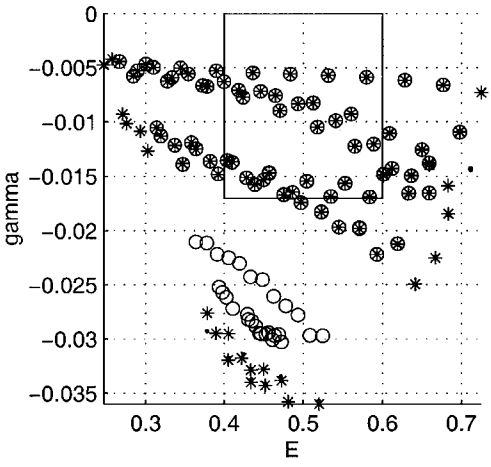

FIG. 18. This calculation uses $\hbar = 0.017$ and $\alpha \in \{0.0425, 0.0599, 0.0774\}$. It was done on a 149×159 grid, and 127 out of $N = 23{,}691$ eigenvalues were computed.

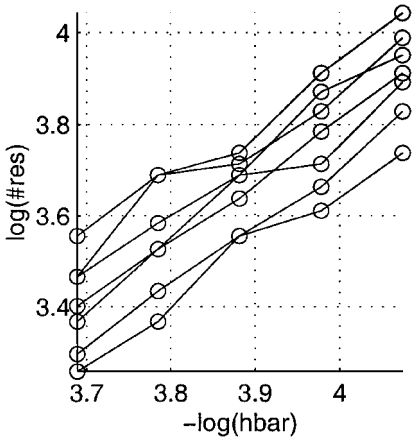

FIG. 19. This plot shows $\log(N_{\text{res}})$ as a function of $-\log(\hbar)$, for $\hbar$ varying from 0.017 to 0.025 and $R \in \{1.4, 1.45, 1.5, \ldots, 1.7\}$: The bottom curve corresponds to $R = 1.7$, while the top curve corresponds to $R = 1.4$.

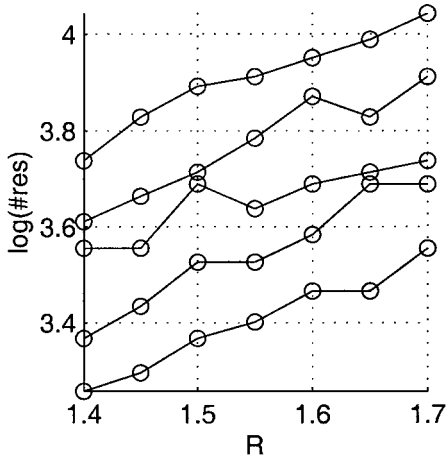

FIG. 20. This plot shows $\log(N_{\text{res}})$ as a function of R, for different values of $-\log(\hbar)$: The top curve corresponds to $\hbar = 0.017$, while the bottom curve corresponds to $\hbar = 0.025$. (The values of $\hbar$ form a geometric sequence.)

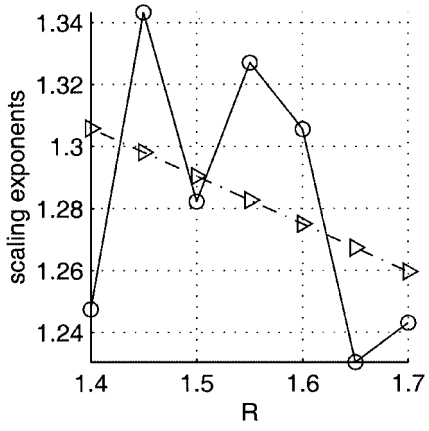

FIG. 21. The slopes extracted from Fig. 19, as a function of R. The dotted curve is a least-squares linear fit of the "noisy" curve.

interest were computed. Notice the cluster of eigenvalues near the bottom edge of the plots. These are *not* resonances because they vary under perturbations in α. Instead, they belong to an approximation of the (scaled) continuous spectrum.

It is more interesting to see $\log(N_{\text{res}})$ as a function of $-\log(\hbar)$ and R. This is shown in Figs. 19 and 20. Using least-squares regression, we can extract approximate slopes for the curves in Fig. 19; these are shown in Table II and plotted in Fig. 21.

6.2. Trapped Set Dimension

For comparison, $\frac{D(K_E)+1}{2}$ is plotted as a function of R in Fig. 22. The figure contains curves corresponding to different energies E: The top curve corresponds to $E = 0.4$, the

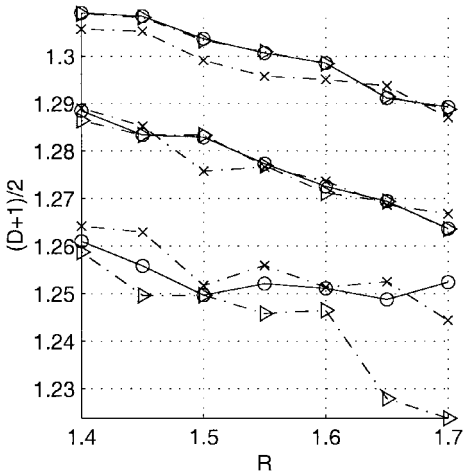

FIG. 22. This figure shows $\frac{D(K_E)+1}{2}$ as a function of R: The top group of curves have $E = 0.4$, the middle $E = 0.5$, and the bottom $E = 0.6$. Solid curves marked with circles represent computations where $N = 10{,}000$, $N' = 100$, $\frac{2\pi}{3} \le \theta \le \frac{4\pi}{3}$, and $-\frac{1}{2} \le p_\theta \le \frac{1}{2}$. Dashed curves marked with Xs represent computations where $N = 14{,}142$, whereas dashed curves marked with triangles represent computations where $N = 10{,}000$ and $N' = 71$. The recursion depth k_0 in all these figures is 6. The $E = 0.6$ curve does not appear to have completely converged but suffices for our purpose here.

TABLE I
Estimates of $\frac{D(K_E)+1}{2}$ as a Function of R

R	$E=0.4$	$E=0.5$	$E=0.6$
1.4	1.3092	1.2885	1.261
1.45	1.3084	1.2834	1.2558
1.5	1.3037	1.2829	1.2497
1.55	1.3007	1.2773	1.2521
1.6	1.2986	1.2725	1.2511
1.65	1.2912	1.2694	1.2488
1.7	1.2893	1.2636	1.2524

middle curve $E=0.5$, and the bottom curve $E=0.6$. It also contains curves corresponding to different program parameters, to test the numerical convergence of dimension estimates. These curves were computed with $\theta \in [\frac{2\pi}{3}, \frac{4\pi}{3}]$, $p_\theta \in [-\frac{1}{2}, \frac{1}{2}]$, and recursion depth $k_0=6$ (corresponding to symmetric sequences of length $2\cdot 6+1=13$); the caption contains the values of N and N' for each curve. For reference, Table I contains the dimension estimates shown in the graph. It is important to note that, while the dimension does depend on E and R, it only does so weakly: Relative to its value, $\frac{D(K_E)+1}{2}$ is very roughly constant across the range of R and E computed here.

6.3. Discussion

Table II contains a comparison of $\frac{D(K_E)+1}{2}$ (for $E=0.5$) as a function of R, versus the scaling exponents from Fig. 21. Figure 23 is a graphical representation of similar information. This figure shows that even though the scaling curve in Fig. 21 is noisy, its trend nevertheless agrees with the conjecture. Furthermore, the relative size of the fluctuations is small. At the present time, the source of the fluctuation is not known, but it is possible that the range of $\hbar$ explored here is simply too large to exhibit the asymptotic behavior clearly. They may also reflect irregularities in the smoothness of the function $1/T$ near the trapped set; see Footnote 2.

Figures 24–30 contain plots of $\log(N_{\text{res}})$ versus $-\log(\hbar)$, for various values of R. Along with the numerical data, the least-squares linear fit and the scaling law predicted by the

TABLE II
Slopes Extracted from Fig. 19

R	Slope	$\frac{D(K_{0.5})+1}{2}$	Relative error
1.4	1.2475	1.2885	0.032888
1.45	1.3433	1.2834	0.044645
1.5	1.2822	1.2829	0.00052244
1.55	1.327	1.2773	0.037472
1.6	1.3055	1.2725	0.025256
1.65	1.2304	1.2694	0.031756
1.7	1.2431	1.2636	0.016509

Note. Relative errors are also shown.

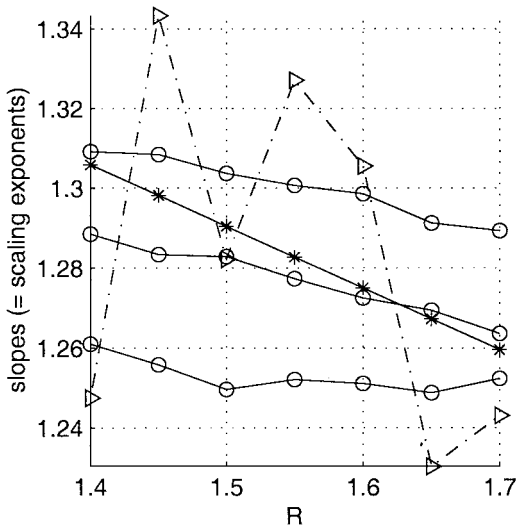

FIG. 23. Dashed lines with circles represent $\frac{D(K_E)+1}{2}$ as functions of R, for $E \in \{0.4, 0.5, 0.6\}$. The dotted curve with triangles is the scaling exponent curve from Fig. 21, while the solid curve with stars is the linear regression curve from that figure. Relative to the value of the dimension, the fluctuations are actually fairly small. See Table II for a quantitative comparison.

conjecture are also plotted.[8] In contrast with Fig. 23, these show clear agreement between the asymptotic distribution of resonances and the scaling exponent predicted by the conjecture.

6.4. Double Gaussian Scattering

Finally, let us examine resonances for the double gaussian model (setting $m = 2$ in (7). This case is interesting for two reasons: First, there exist rigorous results [14, 22] against which we can check the correctness of our results. Second, it helps determine the validity of semiclassical arguments for the values of $\hbar$ used in computing resonances for the triple gaussian model.

The resonances are shown in Figs. 31–37: In these plots, $R = 1.4$ and $\hbar$ ranges from 0.035 to 0.015. One can observe apparent pseudospectral effects in the first few figures [31, 37]; this is most likely because the scaling angle α used here is twice as large as suggested in Section 4.1, to exhibit the structure of resonances farther away from the real axis.

To compare this information with known results [14, 22], we need some definitions: For a given energy $0 < E < 1$, define C(E) by

$$C(E) = 2 \int_{x_0(E)}^{x_1(E)} (2 \cdot (E - V(x)))^{1/2} \, dx, \tag{52}$$

[8] The conjecture only supplies the exponents for power laws, not the constant factors. In the context of these logarithmic plots, this means the conjecture gives us only the slopes, not the vertical shifts. It was thus necessary to compute an y-intercept for each "prediction" curve (for the scaling law predicted by the conjecture) using least squares.

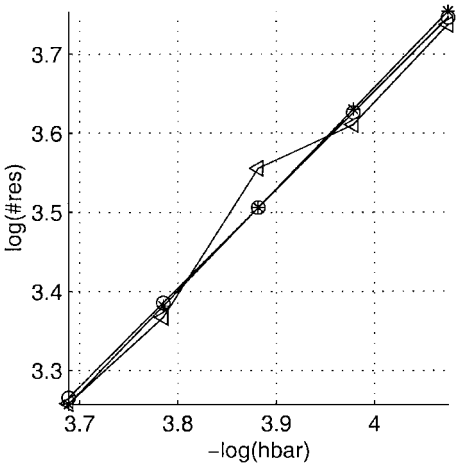

FIG. 24. This plot shows $\log(N_{\text{res}})$ as a function of $-\log(\hbar)$, for $R = 1.4$. Triangles represent resonance counting data, circles represent a least squares fit of the resonance data, and stars represent the exponents predicted by the conjecture. In this plot, $\hbar$ varies geometrically from 0.025 down to 0.017.

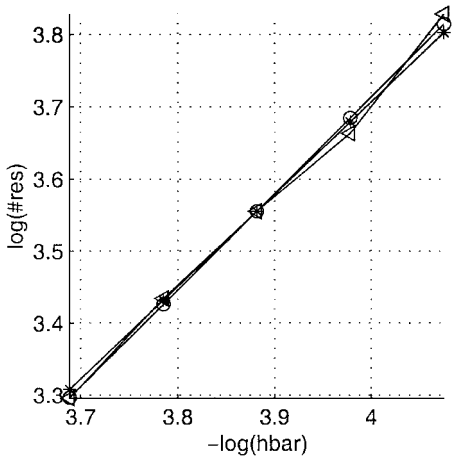

FIG. 25. The same plot, but for $R = 1.45$.

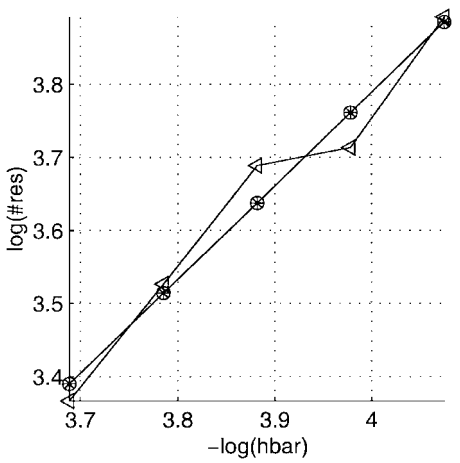

FIG. 26. The same plot, but for $R = 1.5$.

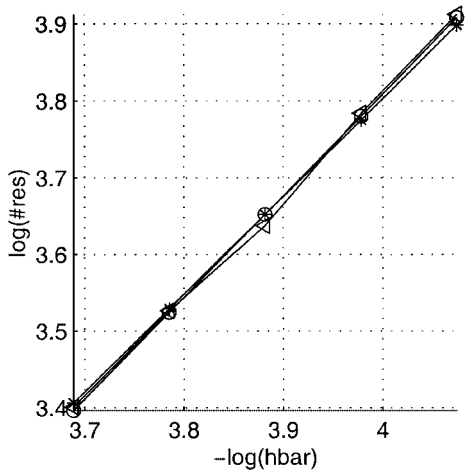

FIG. 27. The same plot, but for $R = 1.55$.

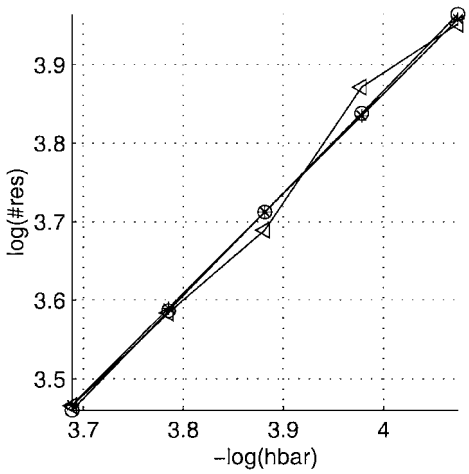

FIG. 28. The same plot, but for $R = 1.6$.

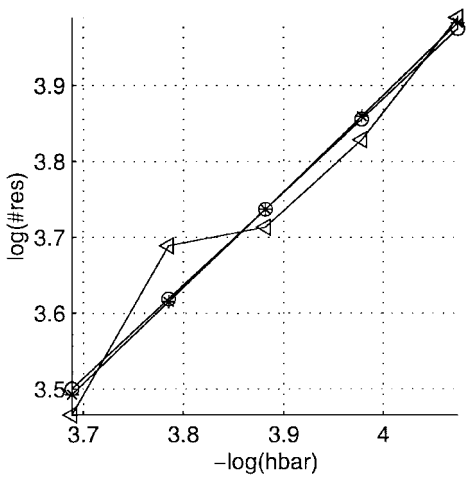

FIG. 29. The same plot, but for $R = 1.65$.

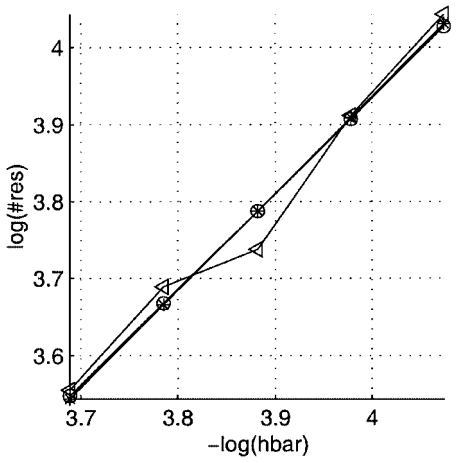

FIG. 30. The same plot, but for $R = 1.7$.

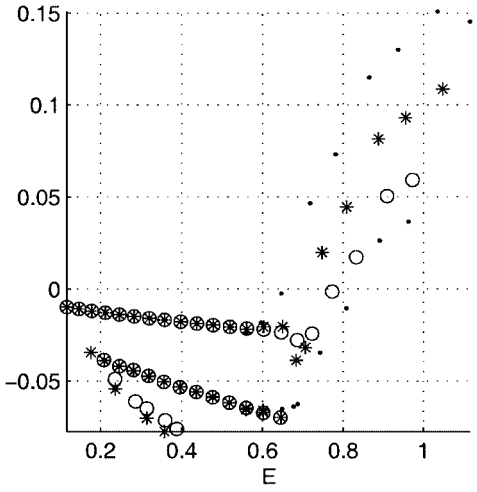

FIG. 31. Resonances for two-bump scattering with $\hbar = 0.035$. As before, filled circles mark resonances, while stars, empty circles, and dots mark other eigenvalues of $\hat{H}_\alpha$. Note apparent pseudospectral effects (see Section 4.1).

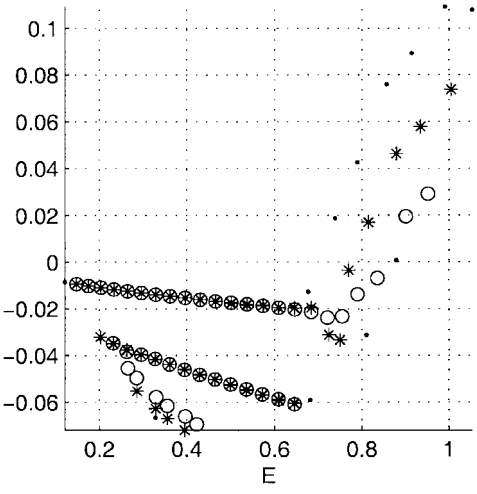

FIG. 32. Resonances for two-bump scattering with $\hbar = 0.030391$.

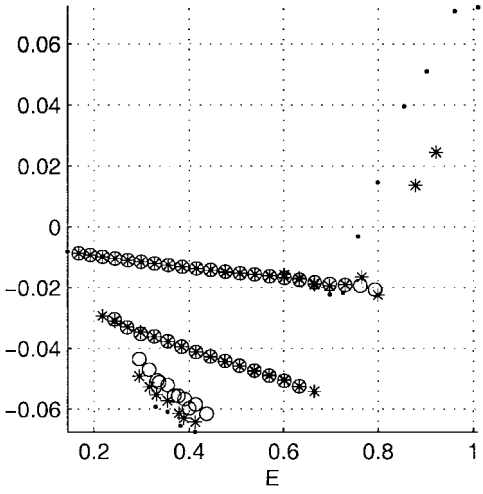

FIG. 33. Resonances for two-bump scattering with $\hbar = 0.026388$.

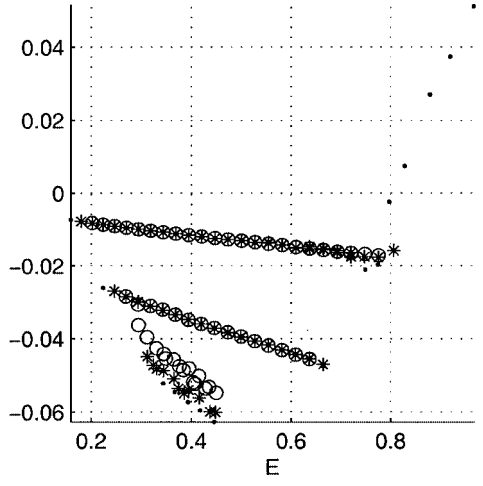

FIG. 34. Resonances for two-bump scattering with $\hbar = 0.022913$.

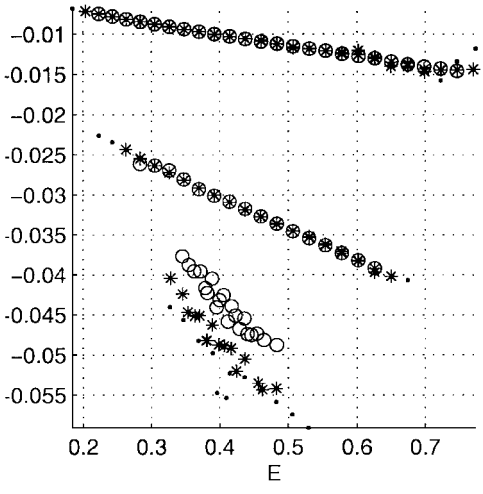

FIG. 35. Resonances for two-bump scattering with $\hbar = 0.019895$.

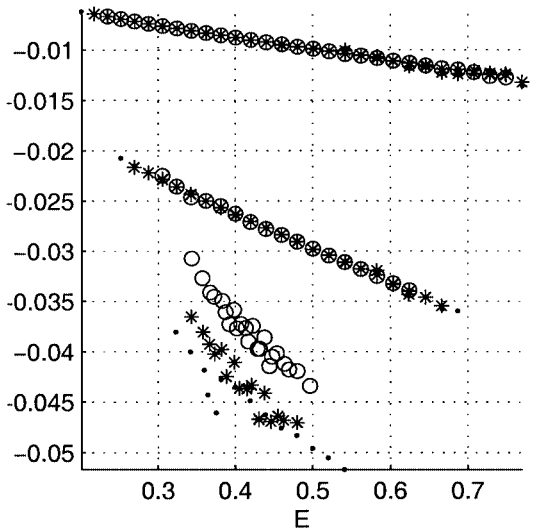

FIG. 36. Resonances for two-bump scattering with $\hbar = 0.017275$.

where the limits of integration are

$$\begin{aligned} x_0(E) &= -R + (-2\sigma^2 \log(E))^{1/2}, \\ x_1(E) &= R - (-2\sigma^2 \log(E))^{1/2}. \end{aligned} \tag{53}$$

Let $\theta(E)$ denote the larger (in absolute value) eigenvalue of $D\tilde{\Phi}(0,0)$; $\log(\theta)$ is the Lyapunov exponent of $\tilde{\Phi}$, and is easy to compute numerically in this case. Note that for two-bump scattering, each energy E determines a unique periodic trapped trajectory, and $C(E)$ is the classical action computed along that trajectory.

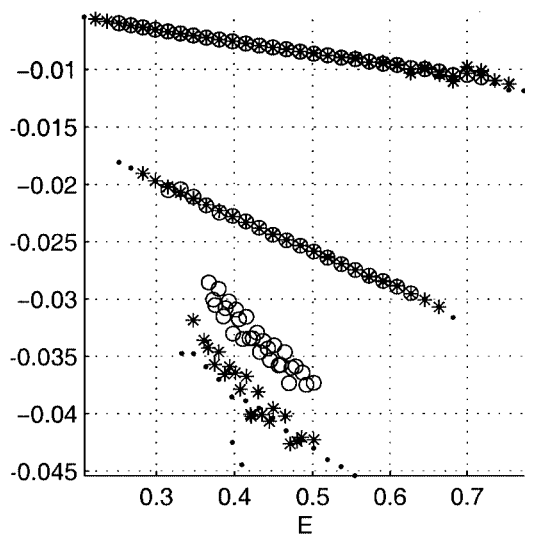

FIG. 37. Resonances for two-bump scattering with $\hbar = 0.015$.

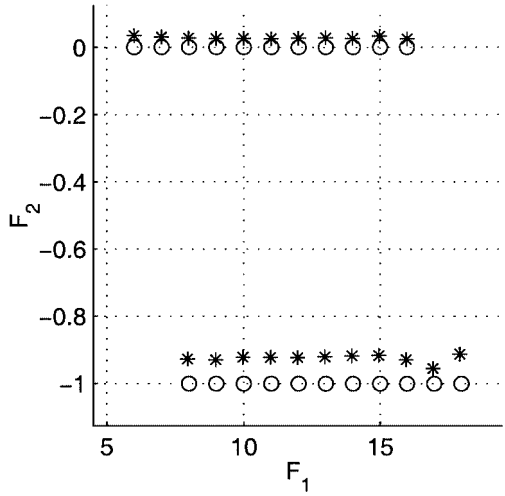

FIG. 38. Lattice points for $\hbar = 0.035$.

Since these expressions are analytic, they have continuations to a neighborhood of the real line: The limits $x_0(\lambda)$ and $x_1(\lambda)$ are calculated using the natural branch of the square root, so that $(a+ib)^{1/2} = a^{1/2} + iba^{-1/2} + O(b^2)$. The function $C(\lambda)$ is then computed along the straight line connecting x_0 to x_1 (though Cauchy's theorem tells us that any nearby contour will do). In [14], it was shown that any resonance $\lambda = E - i\gamma$ must satisfy

$$C(\lambda) = 2\pi\hbar\left(m + \frac{1}{2}\right) - i\hbar\left(n + \frac{1}{2}\right)\log(\theta(\mathrm{Re}(\lambda))) + O(\hbar^2), \tag{54}$$

where m and n are nonnegative integers. (The $\frac{1}{2}$ in $m + \frac{1}{2}$ comes from the Maslov index associated with the classical turning points.) This suggests that we define the map

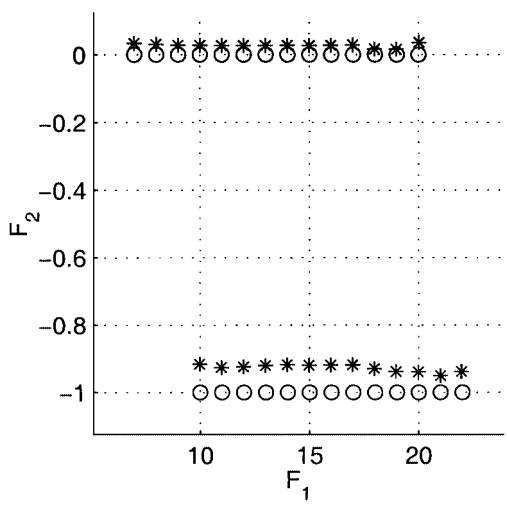

FIG. 39. Lattice points for $\hbar = 0.030391$.

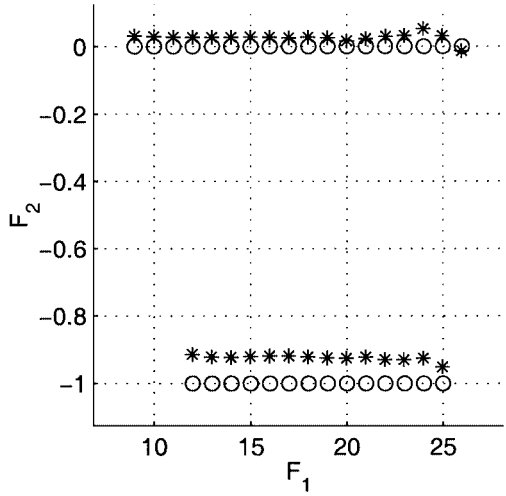

FIG. 40. Lattice points for $\hbar = 0.026388$.

$F(\lambda) = (F_1(\lambda), F_2(\lambda))$, where

$$F_1(\lambda) = \frac{\mathrm{Re}(C(\lambda))}{2\pi\hbar} - \frac{1}{2} \tag{55}$$

and

$$F_2(\lambda) = \frac{\mathrm{Im}(C(\lambda))}{\hbar \log(\theta(\mathrm{Re}(\lambda)))} + \frac{1}{2}. \tag{56}$$

F should map resonances to points on the square integer lattice, and this is indeed the case: Figures 38–44 contain images of resonances under F, with circles marking the nearest lattice points. The agreement is quite good, in view of the elimination of $O(\hbar^2)$ terms from Eq. (54).

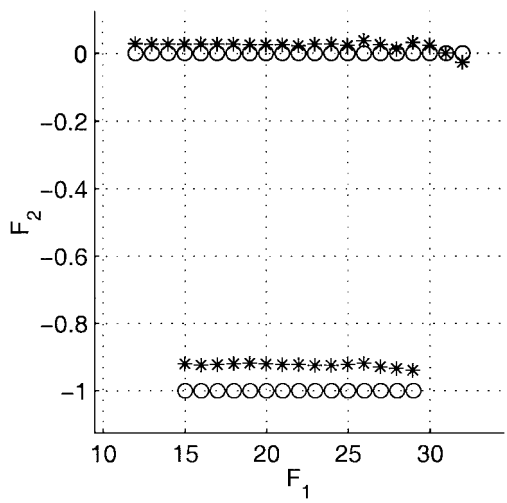

FIG. 41. Lattice points for $\hbar = 0.022913$.

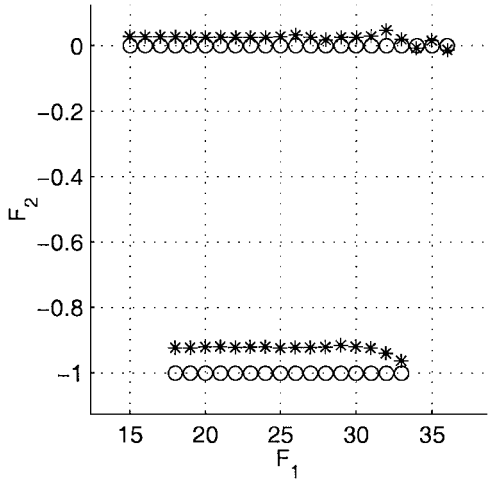

FIG. 42. Lattice points for $\hbar = 0.019895$.

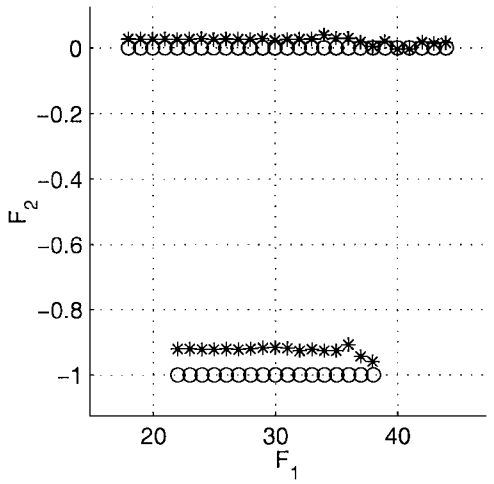

FIG. 43. Lattice points for $\hbar = 0.017275$.

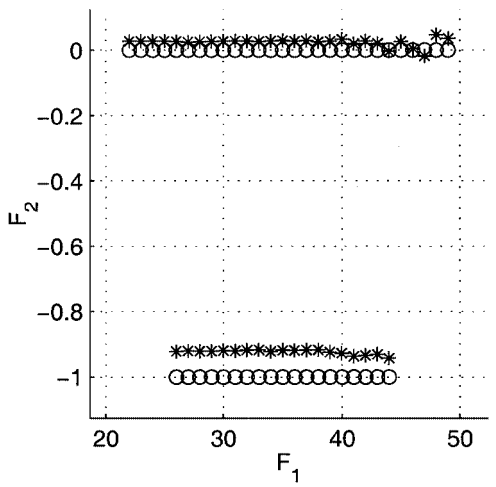

FIG. 44. Lattice points for $\hbar = 0.015$.

7. CONCLUSIONS

Using standard numerical techniques, one can compute a sufficiently large number of resonances for the triple gaussian system to verify their asymptotic distribution in the semiclassical limit $\hbar \to 0$. This, combined with estimates of the fractal dimension of the classical trapped set, gives strong evidence that the number of resonances N_{res} in a box $[E_0, E_1] - i[0, \hbar]$, for sufficiently small $|E_1 - E_0|$ and $\hbar$, satisfies

$$N_{\text{res}} \sim \hbar^{-\frac{D(K_E)+1}{2}}, \tag{57}$$

as one can see in Fig. 23 and Table II. Furthermore, the same techniques, when applied to double gaussian scattering, produce results which agree with rigorous semiclassical results. This supports the correctness of our algorithms and the validity of semiclassical arguments for the range of $\hbar$ explored in the triple gaussian model. The computation also hints at more detailed structures in the distribution of resonances: In Figs. 14–18, one can clearly see gaps and strips in the distribution of resonances. A complete understanding of this structure requires further investigation.

While we do not have rigorous error bounds for the dimension estimates, the numerical results are convincing. It seems, then, that the primary cause for our failure to observe the conjecture in a "clean" way is partly due to the size of $\hbar$: If one could study resonances at much smaller values of $\hbar$, the asymptotics may become more clear.

ACKNOWLEDGMENTS

I am grateful to J. Demmel, B. Parlett, and Z. Bai for crucial advice on matrix computations, and to X. S. Li and C. Yang for help with ARPACK. I also thank R. Littlejohn, M. Cargo, and W. H. Miller for suggestions on bases, F. Bonetto for teaching me how to compute fractal dimensions, and C. Pugh and J. Harrison for helpful conversations. In writing this paper, I benefited greatly from the comments of A. J. Chorin and S. Zelditch. Finally, I thank M. Zworski for inspiring this project. This work was supported in part by the Applied Mathematical Sciences subprogram of the Office of Energy Research of the U.S. Department of Energy under Contract DE-AC03-76-SF00098. Computational resources were provided by the Mathematics Department at Lawrence Berkeley National Laboratory, the National Energy Research Scientific Computing Center (NERSC), and the Millennium Project at U. C. Berkeley.

REFERENCES

1. J. Aguilar and J. M. Combes, A class of analytic perturbations for one body Schrödinger Hamiltonians, *Comm. Math. Phys.* **22**, 269 (1971).
2. E. Anderson, Z. Bai, C. Bischof, *et al*., *LAPACK User's Guide,* 3rd. ed. (Soc. for Industr. & Appl. Math., Philadelphia, 1999).
3. V. I. Arnold, *Mathematical Methods of Classical Mechanics* (Springer-Verlag, Berlin/New York, 1989).
4. E. Balslev and J. M. Combes, Spectral properties of many-body Schrödinger operators with dilation analytic interactions, *Comm. Math. Phys.* **22**, 280 (1971).
5. R. Barrett, M. Berry, T. F. Chan, *et al*., *Templates for the Solution of Linear Systems: Building Blocks for Iterative Methods* (Soc. for Industr. & Appl. Math., Philadelphia, 1994).
6. H. A. Bethe and E. E. Salpeter, *Quantum Mechanics of One- and Two-Electron Atoms* (Plenum, New York, 1977).
7. M. J. Davis and E. J. Heller, Semiclassical Gaussian basis set method for molecular vibrational wave functions, *J. Chem. Phys.* **71**, 3383 (1979).

8. M. Dimassi and J. Sjöstrand, *Spectral Asymptotics in the Semi-Classical Limit* (Cambridge Univ. Press, Cambridge, UK, 1999).
9. K. J. Falconer, *Fractal Geometry: Mathematical Foundations and Applications* (Wiley, New York, 1990).
10. P. Gaspard and S. A. Rice, Scattering from a classically chaotic repellor, *J. Chem. Phys.* **90**, 2225 (1989).
11. P. Gaspard and S. A. Rice, Semiclassical quantization of the scattering from a classically chaotic repellor, *J. Chem. Phys.* **90**, 2242 (1989).
12. P. Gaspard and S. A. Rice, Exact quantization of the scattering from a classically chaotic repellor, *J. Chem. Phys.* **90**, 2255 (1989).
13. P. Gaspard, *Chaos, Scattering, and Statistical Mechanics* (Cambridge Univ. Press, Cambridge, UK, 1998).
14. C. Gérard and J. Sjöstrand, Semiclassical resonances generated by a closed trajectory of hyperbolic type, *Comm. Math. Phys.* **108**(3), 391 (1987).
15. L. Guillopé and M. Zworski, Wave trace for Riemann surfaces, *Geom. Funct. Anal.* **6**, 1156 (1999).
16. I. P. Hamilton and J. C. Light, On distributed Gaussian bases for simple model multidimensional vibrational problems, *J. Chem. Phys.* **84**, 306 (1986).
17. M. Kac, Can one hear the shape of a drum? *Am. Math. Mon.* **73**(4), 1 (1966).
18. A. Knauf, The n-centre problem of celestial mechanics, preprint (2000).
19. A. Lahmar-Benbernou and A. Martinez, On Helffer-Sjöstrand's theory of resonances, preprint `mp_arc 01-104` (2001).
20. R. B. Lehoucq, D. C. Sorensen, and C. Yang, *ARPACK User's Guide: Solution of Large-Scale Eigenvalue Problems with Implicitly Restarted Arnoldi Methods* (Soc. for Industr. & Appl. Math., Philadelphia, 1998).
21. J. C. Light, I. P. Hamilton, and J. V. Lill, Generalized discrete variable approximation in quantum mechanics, *J. Chem. Phys.* **82**, 1400 (1985).
22. W. H. Miller, Classical-limit Green's function (fixed-energy propagator) and classical quantization of non-separable systems, *J. Chem. Phys.* **56**(1), 38 (1972).
23. W. H. Miller, Tunneling and state specificity in unimolecular reactions, *Chem. Rev.* **87**, 19 (1987).
24. Ya. B. Pesin, *Dimension Theory in Dynamical Systems: Contemporary Views and Applications* (Univ. of Chicago Press, Chicago, 1997).
25. T. N. Rescigno, M. Baertschy, W. A. Isaacs, and C. W. McCurdy, Collisional breakup in a quantum system of three charged particles, *Science* **286**, 2474 (1999).
26. W. McC. Siebert, *Circuits, Signals, and Systems* (MIT Press, Cambridge, MA, 1986).
27. B. Simon, The definition of molecular resonance curves by the method of exterior complex scaling, *Phys. Lett. A* **71**, 211 (1979).
28. J. Sjöstrand, Geometric bounds on the density of resonances for semi-classical problems, *Duke Math. J.* **60**, 1 (1990).
29. J. Sjöstrand and M. Zworski, Complex scaling and the distribution of scattering poles, *J. Am. Math. Soc.* **4**, 729 (1991).
30. G. J. Sussman, J. Wisdom, and M. E. Mayer, *Structure and Interpretation of Classical Mechanics* (MIT Press, Cambridge, MA, 2001).
31. L. N. Trefethen, Pseudospectra of linear operators, *SIAM Rev.* **39**(3), 383 (1989).
32. B. A. Waite and W. H. Miller, Model studies of mode specificity in unimolecular reaction dynamics, *J. Chem. Phys.* **73**, 3713 (1980).
33. B. A. Waite and W. H. Miller, Mode specificity in unimolecular reaction dynamics: the Hénon-Heiles potential energy surface, *J. Chem. Phys.* **74**, 3910 (1981).
34. M. Wei, G. Majda, and W. Strauss, Numerical computation of the scattering frequencies for acoustic wave equations, *J. Comput. Phys.* **75**, 345 (1988).
35. A. Wirzba, Quantum mechanics and semiclassics of hyperbolic n-disk scattering systems, *Phys. Rep.* **309**, 1–2 (1999).
36. M. Zworski, Dimension of the limit set and the density of resonances for convex co-compact hyperbolic surfaces, *Invent. Math.* **136**, 353 (1999).
37. M. Zworski, Numerical linear algebra and solvability of partial differential equations, preprint (2001).
38. M. Zworski, Resonances in geometry and physics, *Not. AMS* **319** (March 1999).